

# Two-stage deep learning framework for the restoration of incomplete-ring PET images

Yeqi Fang\* and Rong Zhou

College of Physics, Sichuan University, Chengdu 610065, China

## Abstract

Positron Emission Tomography (PET) is an important molecular imaging tool widely used in medicine. Traditional PET systems rely on complete detector rings for full angular coverage and reliable data collection. However, incomplete-ring PET scanners have emerged due to hardware failures, cost constraints, or specific clinical needs. Standard reconstruction algorithms often suffer from performance degradation with these systems because of reduced data completeness and geometric inconsistencies. We present a two-stage deep-learning framework that, without incorporating any time-of-flight (TOF) information, restores high-quality images from data with about 50% missing coincidences—double the loss levels previously addressed by CNN-based methods. The pipeline operates in two stages: a projection-domain Attention U-Net first predicts the missing sections of the sinogram by leveraging spatial context from neighbouring slices, after which the completed data are reconstructed with OSEM algorithm and passed to an adaptive U-Net–diffusion module. This module dynamically adjusts denoising timesteps based on global image quality, efficiently removing residual artefacts while reinstating high-frequency details. Using 206 brain volumes from the Department of Radiology of West China Fourth Hospital, the result shows that our model successfully preserves most anatomical structures and tracer distribution features with PSNR of 35.92 dB and SSIM of 0.9918. Our two-stage deep-learning framework effectively restores high-quality PET images from over 50 % incomplete-ring data, achieving near-complete anatomical fidelity and robust performance without requiring TOF information.

**Keywords:** Incomplete-ring, Sinogram restoration, Attention U-Net, Diffusion-based refinement

## 1 Introduction

Positron emission tomography (PET) is a powerful molecular imaging technique that provides quantitative visualization of metabolic processes within living tissue [1, 2, 3, 4, 5]. PET operates on the principle that positrons annihilate upon encountering electrons, producing detectable 511keV photon pairs: a radiotracer introduces positrons that annihilate upon encountering electrons, and then produce pairs of 511keV photons traveling in opposing directions. The photon pairs are then detected by a pair of scintillation sensors, and each coincidence event will define a line-of-response (LOR). Traditional PET systems usually use complete 360° detector rings to maximize their sensitivity and angular coverage [1].

However, incomplete-ring systems have emerged from practical necessity rather than theoretical preference: they reduce costs and complexity, allow closer access to patients in specialized applications like breast scanning or in-beam therapy monitoring [6], create "open" configurations that alleviate claustrophobia [7, 8], and enable novel applications such as dual-panel brain imaging systems [9]. The trade-off is substantial—incomplete angular coverage creates gaps in projection data, turning reconstruction

---

\*Email: fangyeqi@stu.scu.edu.cn

into an underdetermined problem. Missing angular views inevitably introduce artifacts and resolution non-uniformity [10, 6]. Even time-of-flight capabilities, which partially fix these problems, can't fully compensate for limited view angles [6, 8].

Researchers have investigated various methods to achieve progressive improvements in incomplete-ring PET reconstruction. Analytical ways like filtered back-projection falter immediately—their assumption of complete data leads to pronounced streak artifacts [10]. Iterative approaches like maximum-likelihood expectation-maximization (MLEM) are better by modeling the acquisition process [11], but they still have artifacts along missing view directions [9]. Penalized likelihood methods incorporating prior constraints show promise, as Zhang *et al.* demonstrated by using high-quality prior images to enhance contrast recovery in a dual-panel head-and-neck PET system [9]. And sinogram completion approaches attempt to estimate or interpolate the absent projection data prior to reconstruction [12]. However, these methods remain insufficient to solve the fundamental problem.

Deep learning has shown remarkable success in many fields [13, 14, 15]. Regression-based networks have shown promise in low-dose PET denoising and partial data reconstruction [16] by learning direct mappings between degraded and high-quality images. Liu *et al.*'s U-Net approach to transform artifact-degraded partial-ring PET images [17] demonstrated initial success, but the model in this work is mainly targeted for mild data loss and training data didn't consider the context of sinograms. However, current available techniques have some drawbacks. For examples, while GAN approaches are good at generating visually compelling reconstructions, [18] they are unstable when training and often highly sensitive to hyperparameters, which limit their clinical use. Methods based on explicit likelihood modeling—like VAEs and flow-based approaches—offer solid theoretical foundations. But they usually lose details in reconstructed images and their low speeds also make them not suitable for clinical use. Model-based deep learning frameworks and generative models [19, 20] show promise but risk introducing hallucinated features—a dangerous proposition in medical imaging.

While incomplete-ring PET systems find their primary applications in specialized scenarios such as breast imaging and in-beam therapy monitoring, brain PET imaging also presents compelling use cases for partial-ring designs. Dual-panel brain imaging systems offer reduced claustrophobia for patients while maintaining diagnostic quality. Additionally, open-configuration brain scanners enable better patient access for interventional procedures and real-time monitoring during treatments. More importantly, brain PET serves as an ideal testbed for developing and validating incomplete-ring reconstruction algorithms due to its well-characterized anatomy and the availability of standardized datasets. The complex cerebral structures provide a rigorous evaluation framework for sinogram completion methods, while the high contrast between gray matter, white matter, and CSF regions allows for sensitive assessment of reconstruction artifacts. The techniques developed and validated on brain data can subsequently be adapted to other anatomical regions where incomplete-ring designs offer specific clinical advantages.

In this work we introduce a two-stage deep-learning framework that restores highly degraded partial-ring PET data and, for the first time, is validated under  $> 50\%$  coincidence loss. Our contributions are four-fold: (1) we propose a five-channel slice-stacking strategy that fuses immediate spatial and axial neighbours in the sinogram, providing rich local context for projection restoration; (2) missing-angle gaps are reconstructed with an Attention U-Net specifically tuned for severe angular deficits, enabling the network to focus selectively on informative sinogram regions; (3) the resulting OSEM images are passed to a lightweight residual-diffusion module that iteratively synthesises high-frequency details while suppressing artefacts, thereby decoupling data completion from perceptual refinement; and (4) we establish the first systematic benchmark on 206 brain volumes with half the coincidences removed, demonstrating that our pipeline achieves 35.92 dB / 0.9918 SSIM in image space.

The remainder of this thesis is organized as follows: **Section 2** provides an overview of PET and its basic physics like principles of coincidence detection, and the main problems caused by incomplete rings. We also summarize classical and modern reconstruction methods. **Section 3** presents our contribution in full: the simulation framework for complete and partial rings, the projection-completion Attention U-Net, the subsequent OSEM reconstruction, and the diffusion-based image-refinement module, together with implementation and training details. **Section 4** reports quantitative and qualitative evaluations on 206 brain volumes under several angular-loss patterns, comparing sinogram restoration, preliminary OSEM images and final refined outputs. **Section 5** summarizes our findings by analysing metrics of model performance on test dataset, and discusses limitations and directions for future improvements. **Appendices** provide additional experiments, extended qualitative results, and tables of hyperparameters used in the study.

## 2 System Model and Dataset

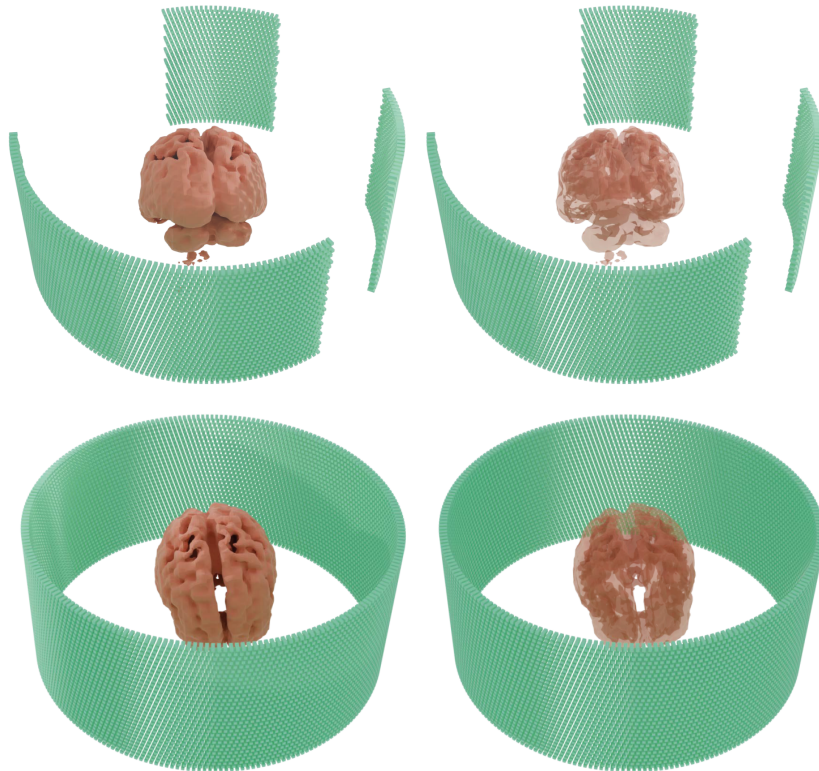


Figure 1: Three-dimensional schematic of incomplete and complete ring PET scanner detector structure, with the right image showing a perspective view.

Incomplete ring configurations arise from practical constraints including cost limitations, hardware failures, and specific clinical requirements. Budget constraints often drive this compromise—each detector module constitutes a substantial cost, and reducing their number can make PET technology accessible to more facilities. In specialized applications, partial ring designs actually provide benefits: breast imaging benefits from closer detector positioning, interventional procedures require open scanner designs, and claustrophobic patients experience less anxiety with more open configurations.

To deal with these problems systematically, we made a thorough simulation framework modeling both complete and incomplete PET geometries. Our approach begins with a standard ring configuration of  $R$  axial rings (we used  $R = 42$  in our experiments), each containing  $D = 182$  detectors arranged

cylindrically. The scanner radius ( $\rho$ ) of 253.71 mm balances spatial resolution against sensitivity.

From listmode to sinogram, and from sinogram to reconstruction, the information is constantly losing. So, rather than attempting direct image-domain recovery, we pivoted to a two-stage method—first converting listmode data to sinograms with missing sections, then applying specialized techniques to complete these sinograms before final reconstruction. This approach, while computationally more intensive, provided a more applicable way to solve the missing data problem by retaining as much information as possible from sinogram. For simulation purposes, we mapped a  $128 \times 128 \times 128$  voxel grid to physical space, yielding in-plane voxel dimensions of approximately 2.78 mm.

Table 1 summarises the target configuration of the in-house PET prototype, an incomplete ring system that is currently being assembled in our laboratory. Because several mechanical layouts are still under evaluation, we designed a custom geometry interface for the Monte-Carlo toolkit SimSET[21]. The interface allows any combination of inactive rings or angular gaps to be enabled or disabled at run-time, giving us maximal flexibility while the hardware design is finalised. Once the full-ring list-mode data have been generated, we post-process the coincidences to emulate incomplete geometries: selected detector rings or azimuthal sectors are masked out, and any coincidence that involves at least one inactive crystal is discarded. This two-stage strategy keeps the underlying activity distribution, Poisson statistics and scatter model identical between the reference and degraded datasets, isolating the effect of missing angular information. Importantly, detector-specific sensitivity variations were incorporated by applying crystal-wise efficiency factors (Gaussian spread  $\approx 10\%$  around the nominal sensitivity), ensuring that the coincidence statistics also reflect non-uniform detector response. The attenuation effect of seven tissue types (i.e, brain, bone, muscle, fat and blood) was considered in the simulations and then corrected during the image reconstruction.

Table 1: PET Scanner Configuration Parameters (based on our planned experimental prototype for future validation studies)

<b>Parameter</b>	<b>Value</b>
Radius	253.71 mm
Crystal transaxial spacing	4.02 mm
Crystal axial spacing	5.37 mm
Module axial spacing	37.56 mm
Crystal elements (transaxial)	13
Crystal elements (axial)	7
Transaxial sectors	28
Axial sectors	1
Modules (axial)	6
Crystals per ring	182
Number of rings	42

We used a dataset of 206 brain PET volumes from 206 individual healthy human subjects, each with dimensions of  $128^3$  voxels from the Department of Radiology of West China Fourth Hospital as phantom images for our simulation. The study was approved by the Medical Ethics Committee of West China Fourth Hospital, Sichuan University (Ethical approval number: HXSJ-EC-2,023,043). The study was retrospective. The use of patient information will not adversely affect them, so we waived informed consent, but data confidentiality was ensured. All methods strictly adhered to relevant guidelines and regulations. Each image simulates 2 billion events including both true and scatter events, the detectors detect 560 million events on average and record them in the listmode data. All subjects had normal

brain anatomy without any pathological conditions, ensuring consistent baseline characteristics across the dataset. The dataset exhibits natural anatomical variation typical of healthy adult brains, including differences in brain size, cortical folding patterns, and regional tissue distributions. Each phantom was down-sampled to a matrix of  $128 \times 128 \times 128$  with voxel size of  $2.78 \times 2.78 \times 2.78\text{mm}^3$ . This healthy brain dataset provides a robust foundation for evaluating our reconstruction framework’s performance on normal anatomical structures before extending to pathological cases in future studies.

The complete ring configuration (Figure 1) provides our reference reconstruction  $\mathbf{Y}_A$ , representing the best-case scenario with full angular sampling. For incomplete ring experiments, we selectively remove detectors—either entire rings or angular segments—and generate a degraded reconstruction  $\mathbf{Y}_B$  from the resulting partial data. The striking quality difference between  $\mathbf{Y}_A$  and  $\mathbf{Y}_B$  shows the reconstruction challenge we aim to solve.

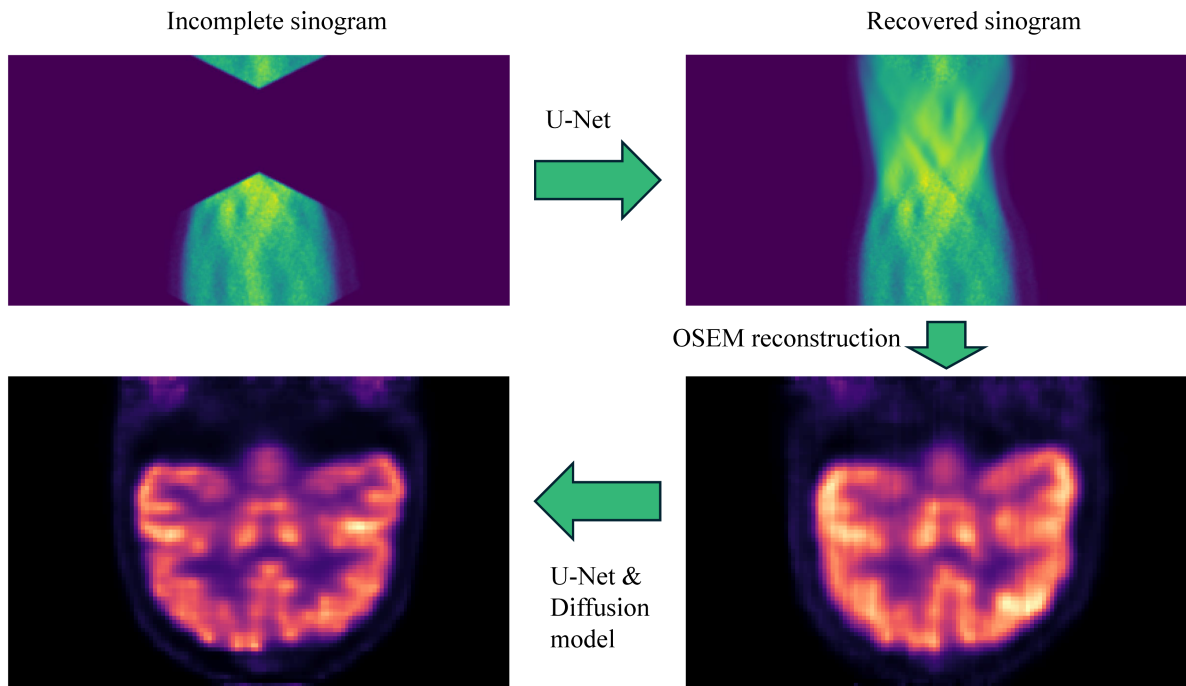


Figure 2: Overall flow diagram of the incomplete ring PET reconstruction method. First, incomplete sinograms due to missing detectors are repaired through a U-Net deep learning model to generate complete sinogram data. Then the complete sinogram is converted into a PET image using the OSEM iterative reconstruction algorithm. Finally, the image is refined using a U-Net & diffusion model to remove residual artifacts and enhance high-frequency details.

### 3 Methods

As shown in Figure 2, this study proposes an innovative incomplete ring PET reconstruction framework that effectively addresses the data incompleteness problem caused by missing detectors through a multi-stage strategy. In the first stage, the system first processes incomplete sinograms (top left) resulting from missing detectors, completing the missing data through a trained optimized U-Net deep learning model to generate complete sinograms (top right). This sinogram restoration process fully utilizes the five-channel input strategy, effectively integrating spatial and temporal context information.

### 3.1 Sinogram Reconstruction Based on Attention U-Net

Sinogram repair is fundamental in incomplete ring PET imaging, as its quality directly affects the precision of reconstructed images. The shape of sinogram tensors is  $(D, 2D + 1, R^2)$ , or  $(182, 365, 1764)$  in our work, where  $R$  is the number of axial rings and  $D$  is the number of detectors each ring. It is evident that this tensor is too large to be directly fed into any UNet-like models. Therefore, we divided this large  $(D, 2D + 1, R^2)$  tensor into  $R \times (D, 2D + 1, R)$  tensors. As shown in Figure 3, the central channel of each input tensor corresponds to the current sinogram slice, while the direct spatial neighbors (slices  $j - 1$  and  $j + 1$ ) and temporal neighbors from previous and subsequent sinogram periods (slices  $j - R$  and  $j + R$ ) constitute the other four channels. For boundary handling, when adjacent indices exceed the dataset range, the central slice itself is used for channel filling, ensuring input dimension consistency. These neighboring slices are important for improving the model’s understanding of local structural continuity and temporal consistency. Consequently, we obtain  $1764 \times (182, 365, 5)$  tensors for each sinogram. To make sure each image was evaluated once in the test set, we implemented 6-fold cross-validation across the 206 volumes (4 groups with 34 images and 2 groups with 35 images). The predictions obtained from our model were reconstructed using the OSEM algorithm to achieve preliminary geometric recovery, and these reconstructions were subsequently used as inputs for our second stage framework.

Although traditional U-Net performs excellently in medical image segmentation and reconstruction tasks [23], it lacks the ability to selectively focus on key features when dealing with complex incomplete ring PET sinogram restoration problems. The Attention U-Net [24] adopted in this study enhances the model’s perception of important feature regions through spatial attention mechanisms while suppressing the influence of irrelevant features, which is more useful for restoring sinograms from incomplete data. We also tested some transformer-based U-Net like UNETR [25], which combines ViT encoder and convolutional decoder, and TransUNet [26], where both encoder and decoder are completely based on transformers. But they are slightly outperformed by Attention U-Net.

The main innovation of Attention U-Net is the introduction of attention gating (AG) modules in the skip connection path of the original U-Net. These AG modules can adaptively highlight significant structures in the feed-forward feature maps while suppressing less relevant regions. For sinogram reconstruction tasks, this mechanism is especially useful as it can selectively focus on structural features around missing areas, and then more accurately infer missing angular data. The mathematical expression of attention gating can be described as [24]:

$$\alpha_i^l = \sigma_2(\psi^T(\sigma_1(W_x^T x_i^l + W_g^T g_i + b_g)) + b_\psi), \quad (1)$$

where  $x_i^l$  is the low-level feature from the encoder,  $g_i$  is the gating signal from the decoder (high-level feature),  $\sigma_1$  and  $\sigma_2$  are ReLU and Sigmoid activation functions respectively, and  $W_x$ ,  $W_g$ ,  $b_g$ , and  $b_\psi$  are learnable parameters.  $\alpha_i^l \in [0, 1]$  is the calculated attention coefficient used to control the importance of features. After processing through the attention gate, the features can be represented as:

$$\hat{x}_i^l = x_i^l \cdot \alpha_i^l. \quad (2)$$

The Attention gates learn to focus on relevant regions of the encoder feature maps by assigning weights based on the context, particularly in cases of severe angular loss. AGs can create a stronger understanding of sinogram continuity and consistency. After testing on our dataset, the results showed that Attention U-Net performs better with an average increase of 1.24dB in PSNR and 0.052 in SSIM compared to original U-Net in sinogram reconstruction tasks. This means that attention mechanism is

more effective in processing incomplete ring PET data.

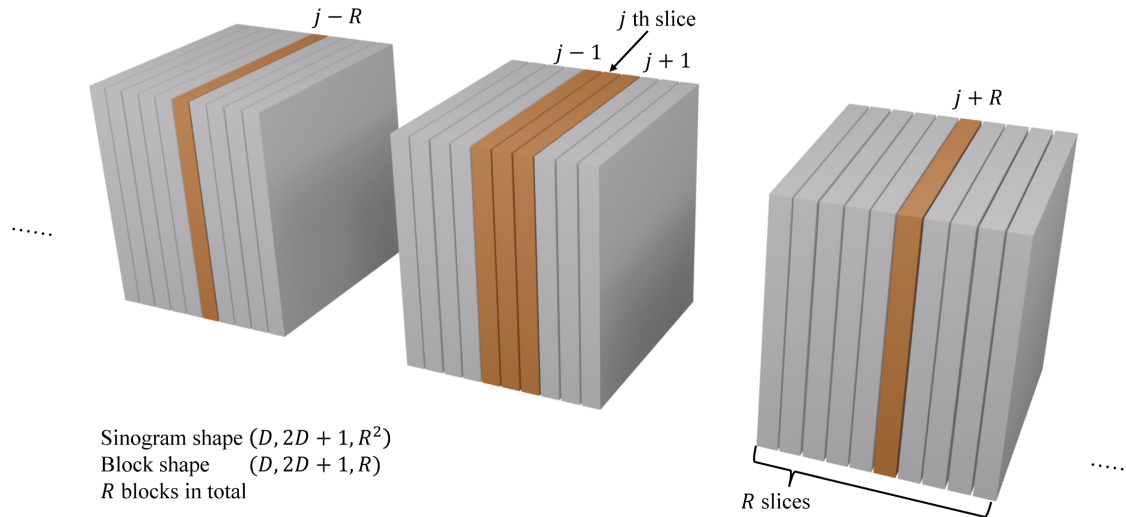


Figure 3: Visualization of the five-channel tensor preparation of sinogram data for training. Each cube represents a sinogram slice block with dimensions  $(D, 2D + 1, R^2)$ . The orange highlighted parts are the selected slices  $(j - R, j - 1, j, j + 1, j + R)$ , which form the five-channel input for the restoration model, showing the spatial and temporal relationships captured in each input tensor.

Model training uses the Adam optimizer with an initial learning rate of  $10^{-4}$  and adds  $10^{-5}$  weight decay to prevent overfitting. Training efficiency is enhanced through mixed precision computation and gradient scaling techniques, combined with a ReduceLROnPlateau dynamic learning rate scheduler (with a decay factor of 0.3 when validation loss shows no improvement for 3 consecutive epochs), achieving stable convergence.

### 3.2 Image Refinement Based on U-Net and Diffusion Model

Then, to further improve the image quality in geometry space, we have the second stage of our framework, which is a dual-model architecture that combines U-Net and diffusion model. The U-Net model is used to generate a coarse prediction of the image, while the diffusion model is used to refine the image by reconstructing the residual signal. This two-stage approach effectively balances reconstruction quality with computational efficiency.

To optimize computational efficiency while maintaining quality, we implement an adaptive denoising strategy that dynamically adjusts diffusion timesteps based on global image quality assessment. During training, we use the standard DDPM (Denoising Diffusion Probabilistic Models) process with  $T_{\text{train}} = 2000$  timesteps to ensure stable learning. However, during inference, we employ the DDIM (Denoising Diffusion Implicit Models) sampling strategy [?] which allows us to achieve comparable quality with significantly fewer timesteps.

Specifically, we compute a global quality score  $Q_{\text{global}}$  using the BRISQUE (Blind/Referenceless Image Spatial Quality Evaluator) metric [?]:

$$Q_{\text{global}} = \text{BRISQUE}(I_{\text{unet}}) \quad (3)$$

where  $I_{\text{unet}}$  represents the U-Net output. BRISQUE provides a perceptual quality score without requiring a reference image. Based on this assessment, the number of DDIM sampling steps  $T_{\text{adaptive}}$  is selected

as:

$$T_{adaptive} = T_{min} + (T_{max} - T_{min}) \cdot \text{sigmoid}(\alpha \cdot Q_{global} - \beta) \quad (4)$$

where  $\alpha = 0.1$  and  $\beta = 30$  are empirically determined scaling parameters, and  $T_{min} = 10$ ,  $T_{max} = 50$ .

And we also use an auxiliary guidance strategy and a contrastive diffusion strategy to improve the reconstruction quality [27]. The auxiliary guidance strategy uses neighboring axial slices and spectral information to provide additional context for the reconstruction, while the contrastive diffusion strategy ensures that the model produces anatomically plausible reconstructions specific to each individual scan. And we train the model using a combination of L1 loss and contrastive loss without pretrained weights.

## 4 Results

In order to investigate the effect of the form of loss on the reconstruction results while ensuring that the total amount of data loss remained constant, we varied the range of angles at which the data were missing and ensured that the total range of missing angles remained constant and repeated the experimental procedure. The results on test set are listed in Table 2. The table includes PSNR and SSIM values of the recovered sinogram data by the first stage Attention U-Net, the reconstruction from these sinogram, and the refined images from the reconstruction using the second stage model. The results indicate that our method achieves high-quality reconstruction performance, with PSNR values exceeding 30 dB and SSIM values above 0.95 for most cases.

Table 2: Quantitative results for different angular-loss patterns

Lost angle range	Parameter	Mean	Std
[30°, 90°] & [210°, 270°]	SSIM (refined)	0.9902	0.01232
	PSNR (refined)	35.36 dB	2.332 dB
	SSIM	0.9703	0.01480
	PSNR	32.12 dB	2.650 dB
	SSIM (sinogram)	0.9827	0.001512
	PSNR (sinogram)	35.98 dB	0.3101 dB
[60°, 120°] & [240°, 300°]	SSIM (refined)	0.9905	0.01302
	PSNR (refined)	34.97 dB	2.231 dB
	SSIM	0.9709	0.0134
	PSNR	32.91 dB	2.532 dB
	SSIM (sinogram)	0.9830	0.001612
	PSNR (sinogram)	35.91 dB	0.2713 dB
[60°, 90°] & [130°, 160°] & [240°, 270°] & [310°, 340°]	SSIM (refined)	0.9918	0.01152
	PSNR (refined)	35.92 dB	2.542 dB
	SSIM	0.9761	0.01315
	PSNR	33.10 dB	2.851 dB
	SSIM (sinogram)	0.9879	0.001349
	PSNR (sinogram)	38.41 dB	0.2629 dB

Figure 4 demonstrates the model’s capability in reconstructing incomplete sinograms. After 40 rounds of training, the model can effectively recover complete sinogram structures from inputs with missing angular data. From the figure, it can be observed that although the input sinogram (left) has large-scale data loss, the model’s predicted sinogram (middle) successfully restores a structure and signal distribution highly similar to the real sinogram (right). This indicates that our proposed two-stage

restoration framework can effectively learn the potential structures and features in sinograms, enabling accurate reconstruction even in cases of severe data loss. Figure 5 shows the PET image quality gen-

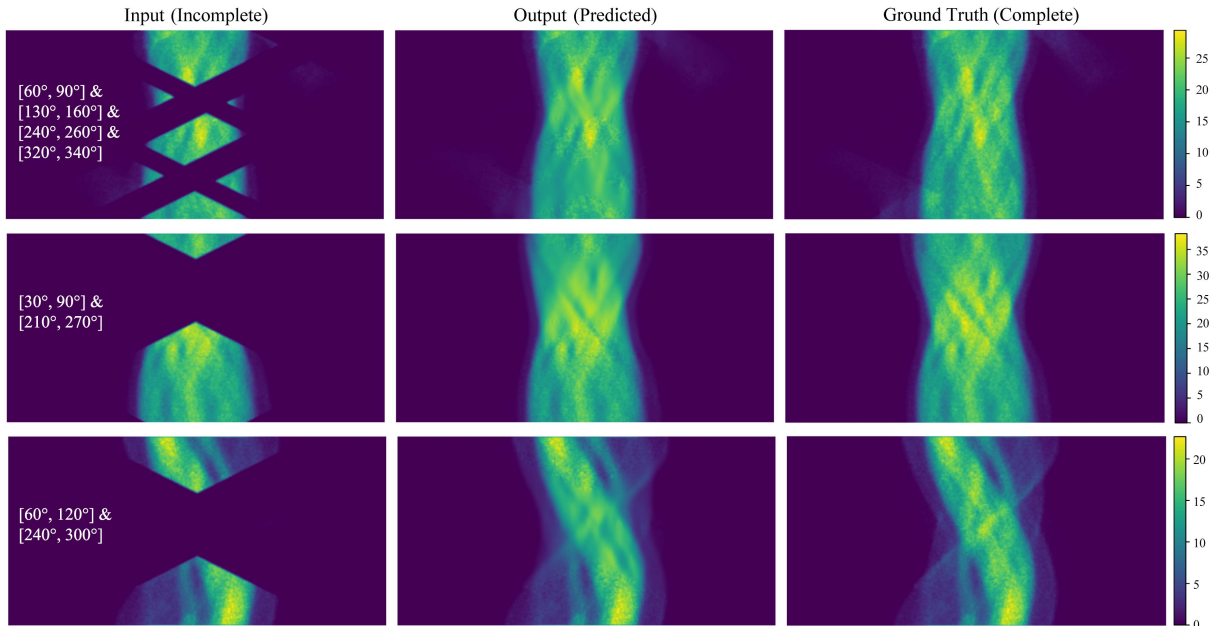


Figure 4: Comparison of PET sinogram reconstruction results after training (metrics are shown in Table 2). Each row displays three images: the left shows the incomplete input sinogram with missing angular data, the middle shows the model-predicted complete sinogram, and the right shows the complete real sinogram. And each row corresponds to a different angular loss range, as indicated in the first column.

erated from the reconstructed sinogram. Its PSNR reached 32.12 dB and SSIM 0.9703. By comparing the original PET brain image (left) with the reconstructed PET image (right), it can be seen that the reconstructed image successfully preserves key anatomical structures and tracer distribution features from the original image. Particularly in the cerebral cortex and basal ganglia regions, the reconstructed image clearly preserves the boundaries and contrast of high uptake areas.

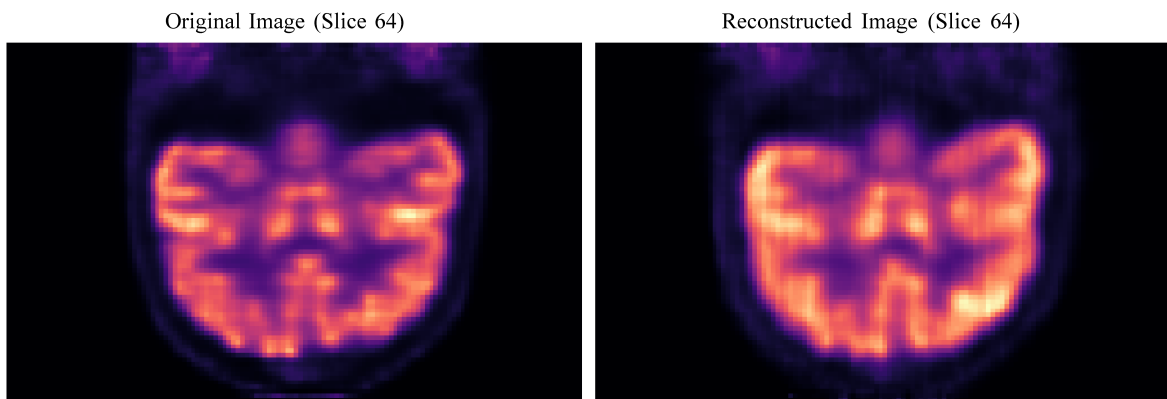


Figure 5: Comparison of original PET brain image (left) with PET image reconstructed from predicted sinogram (right), both showing the 64th layer slice with SSIM of 0.9703 and PSNR of 32.12 dB. The lost angle range is  $[30^\circ, 90^\circ]$  and  $[210^\circ, 270^\circ]$ .

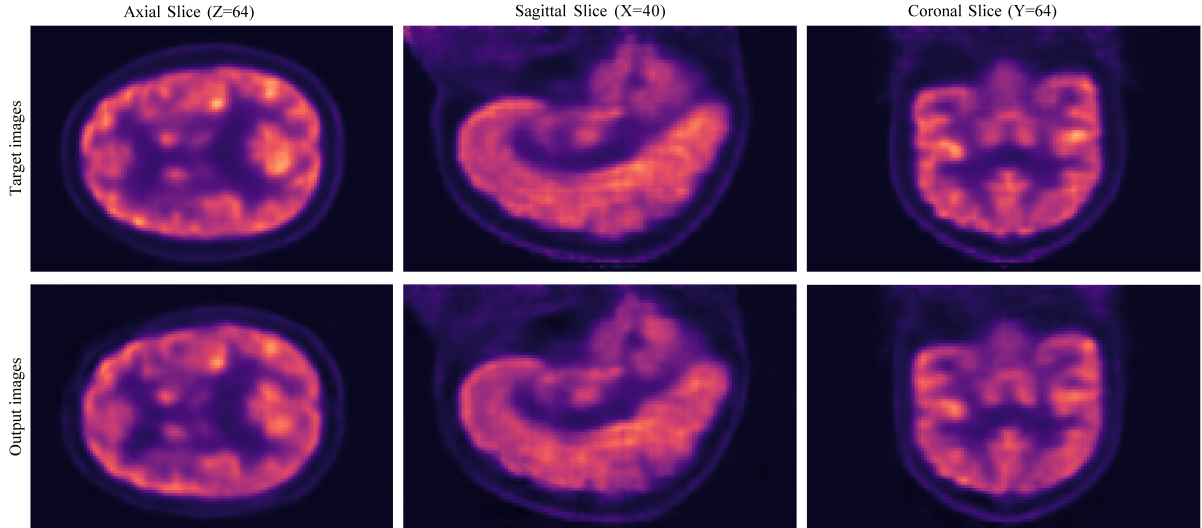


Figure 6: Comparison of original PET brain image (top) with PET image refined from the raw images reconstructed from predicted sinogram (bottom) with the SSIM of 0.9902 and PSNR of 35.36 dB. The lost angle range is  $[30^\circ, 90^\circ]$  and  $[210^\circ, 270^\circ]$ . The axial slices should be  $128 \times 128$ , but we only show the central  $128 \times 80$  part.

## 5 Conclusion and Discussion

From the experimental results, we demonstrate that our two-stage reconstruction can effectively recover PET images from incomplete ring geometries. And we also have several important findings. First, our model performs remarkably well despite operating with approximately 50% missing data and 1/3 missing detectors, in which case direct reconstruction without restoration will cause a chaos. But our approach was still able to achieve PSNR values above 30 dB and SSIM scores above 0.97 for images, indicating successful ability to recover missing information of key structural features.

While the total amount of missing data remains constant, the specific distribution of the missing affects the quality of the recovery. The model extrapolates the missing parts with the help of existing data, and when the sinogram contains an entire missing region, the model will infer the missing parts from farther away, which will lead to a decrease in the quality of recovery, as shown in the second and third rows of Figure 4. However, when the missing and intact parts are interleaved, the quality of recovery improves because the model is able to extrapolate from a closer and thus more accurate location.

Additionally, we also found that attention mechanism is essential for the model to learn the relationship between different parts of the sinogram regardless of distances between them. Comparing the second and third rows of Figure 4, we can observe different patterns of missing data. In the third row, the missing portions are primarily concentrated in the middle region of the sinogram, with relatively balanced data preserved in both the upper and lower sections. In contrast, the second row’s missing data extends closer to the upper part of the sinogram, with only a narrow band of preserved data in the upper region. So if the model can only capture short distance relationships, the second row will be more difficult to recover than the third row because the model has to extrapolate the missing parts from farther away. However, the results from Table 2 show that the PSNR and SSIM of the second row are actually quite similar to those of the third row. This indicates that the attention mechanism can help the model learn the relationship between different parts of the sinogram regardless of distances between them, which is very important for the model to leverage the existing data effectively to recover the missing parts.

Our dataset with only adjacent slices can solve the memory usage problem when processing super-

large sinogram tensors in a simple way. Instead of processing the whole tensor of the size  $(182, 365, 1764)$  all at a time, we divided it into  $R \times (D, 2D + 1, R)$  tensors and process them sequentially. However, this approach results in loss of the context for each slice. And by inputting five input channels per slice (the current slice, two spatial neighbors, and two temporal neighbors), we created a contextually sufficient representation and also lower memory costs. This approach avoid memory limitations and also enhance reconstruction quality by considering correlated information from adjacent slices, showing an average increase of 1.24dB in PSNR and 0.052 in SSIM compared to single-slice processing.

For more robust evaluation and enough data for the second stage, we used 6-fold cross-validation on our 206 volumes dataset. This validation strategy minimizes the influence of random variation and provides more reliable performance metrics. The cross-validated results confirmed this performance advantages with PSNR of 35.92 dB and SSIM of 0.9918 on the validation set. On the contrary, if we do not use cross validation, we can only use the data on the test set (about 36 images) for both training and testing on the model of the second stage. Because of the data leakage, the prediction on the training set cannot be used for the second stage model

Despite encouraging results, our study has several important limitations. First, the Monte-Carlo data were generated under idealised detector conditions that do not yet reflect the full range of crystal-to-crystal variations observed in commercial scanners, which may curb the method’s immediate transferability. Second, validation was performed only on brain PET scans from a modest cohort of healthy volunteers; performance on other organs or on pathological uptake patterns remains unknown. Third, our network processes 2-D slices augmented by neighbouring information, a compromise that can sacrifice some genuinely three-dimensional context. Fourth, we relied on an in-house simulator that has not yet achieved the community acceptance of packages such as GATE, potentially limiting reproducibility. Finally, the evaluation covered only one scanner radius (253.71 mm); further work is required to understand the model’s behaviour across different geometries and partial-ring layouts.

Looking toward future improvements, several avenues can close these gaps. Collecting list-mode data on physical PET systems—ideally including scanners with deliberately inactive modules—will provide the experimental evidence needed for clinical translation. Broadening the test set to whole-body studies and scans containing lesions will demonstrate wider applicability. Migrating the workflow to a GATE-based simulation pipeline would align the study with established practice and enhance credibility. To preserve inter-slice relationships without incurring a full 3-D memory cost, hybrid approaches that add recurrent or transformer-style attention across slices merit exploration. Introducing physics-informed constraints during training could further narrow the gap between simulated and real acquisitions. Finally, larger and more diverse datasets may unlock the full potential of transformer-driven architectures such as UNETR or TransUNet, which showed only marginal advantages in the present, more limited setting.

## **6 Declarations**

### **Conflict of Interest**

The authors declare that they have no conflict of interest.

### **Data Availability**

The data that support the findings of this study are available from West China Fourth Hospital, but restrictions apply to the availability of these data, which were used under license for the current study,

and so are not publicly available. Data are however available from the corresponding authors upon reasonable request.

### Ethics statement

Studies involving human participants were reviewed and approved by the Medical Ethics Committee of West China Fourth Hospital, Sichuan University. The study was retrospective. The use of patient information will not adversely affect them, so we waived informed consent.

### Competing interests

The authors declare that they have no competing interests.

### Consent for publication

Not applicable.

## 7 Acknowledgments

I would like to express my sincere gratitude to senior students, Xiaoyu Chen for insightful discussions and suggestions. The conclusions and analyses presented in this publication were produced using the following software: Python (Guido van Rossum 1986) [28], Opencv (Intel, Willow Garage, Itseez) [29], Scipy (Jones et al. 2001) [30], PyTorch (Meta AI September 2016) [31], Matplotlib (Hunter 2007) [32] and Seaborn [33].

## Appendix

The parameters of the five-channel U-Net network structure are shown in Table 3. We also have skip connections between the encoder and decoder blocks, which are not shown in the table.

Table 3: Five-channel Attention U-Net backbone

Stage / block(s)	Main ops (per level)	$C_{out}$
Input	—	5
Encoder $\times 4$	[Conv $3 \times 3$ + BN + ReLU] $\times 2$ MaxPool $2 \times 2$	64, 128, 256, 512
Bottleneck	[Conv $3 \times 3$ + BN + ReLU] $\times 2$	1024
Decoder $\times 4$	Upsample ( $\uparrow 2$ ) + skip concat [Conv $3 \times 3$ + BN + ReLU] $\times 2$	512, 256, 128, 64
Output	Conv $1 \times 1$	5

All hyperparameters required to replicate the run are collected in Table 7.

## References

- [1] David W. Townsend, Jonathan P. J. Carney, Jeffrey T. Yap, and Nathan C. Hall. PET/CT today and tomorrow. *Journal of Nuclear Medicine*, 45(1 Suppl):4S–14S, 2004.

Table 4: Numerical hyper-parameters for the stage-2 run

Hyper-parameter	Value	Hyper-parameter	Value
<i>Data</i>		<i>Channel multipliers</i>	
batch_size	12	levels	1, 2, 3, 4
l_resolution (=r)	64	<i>Diffusion process</i>	
<i>U-Net</i>		image_size	128
in_channel	1	$T_{\text{train}}$	2000 (DDPM training)
out_channel	1	$T_{\text{min}}$	10 (DDIM sampling)
inner_channel	64	$T_{\text{max}}$	50 (DDIM sampling)
res_blocks	3	$\beta_{\text{start}}$	$1 \times 10^{-6}$
<i>diffusion model</i>		$\beta_{\text{end,train}}$	0.01
in_channel	2	$\beta_{\text{end,val}}$	0.5
out_channel	1	<i>Optimisation</i>	
inner_channel	32	n_iter	600 000
res_blocks	3	learning rate	0.0002
		EMA decay	0.9999

- [2] Gerd Muehllehner and Joel S Karp. Positron emission tomography. *Physics in Medicine & Biology*, 51(13):R117, 2006.
- [3] Katherine Lameka, Michael D Farwell, and Masanori Ichise. Positron emission tomography. *Handbook of clinical neurology*, 135:209–227, 2016.
- [4] Arvind K Shukla and Utham Kumar. Positron emission tomography: An overview. *Journal of medical physics*, 31(1):13–21, 2006.
- [5] Ronald Nutt. The history of positron emission tomography. *Molecular Imaging & Biology*, 4(1):11–26, 2002.
- [6] Suleman Surti and Joel S. Karp. Design considerations for a limited-angle, dedicated breast TOF-PET scanner. *Physics in Medicine and Biology*, 53(11):2911–2921, 2008.
- [7] Hideaki Tashima, Takatomo Yamaya, Eri Yoshida, Shingo Kinouchi, Masaaki Watanabe, and Eiji Tanaka. A single-ring OpenPET enabling PET imaging during radiotherapy. *Physics in Medicine and Biology*, 57(14):4705–4718, 2012.
- [8] Sangeetha Krishnamoorthy, Boon-Keng K. Teo, Wei Zou, James McDonough, Joel S. Karp, and Suleman Surti. A proof-of-concept study of an in-situ partial-ring time-of-flight PET scanner for proton beam verification. *IEEE Transactions on Radiation and Plasma Medical Sciences*, 5(5):694–702, 2021.
- [9] Hengquan Zhang, Yuli Wang, Jinyi Qi, and Shiva Abbaszadeh. Penalized maximum-likelihood reconstruction for improving limited-angle artifacts in a dedicated head and neck PET system. *Physics in Medicine and Biology*, 65(16):165016, 2020.
- [10] Avinash C. Kak and Malcolm Slaney. *Principles of Computerized Tomographic Imaging*. IEEE Press, 1988.
- [11] Jinyi Qi and Richard M. Leahy. Iterative reconstruction techniques in emission computed tomography. *Physics in Medicine and Biology*, 51(15):R541–R578, 2006.

- [12] Shubhangi Makkar, Siqi Ye, Marina Béguin, Günther Dissertori, Jan Hrbacek, Antony Lomax, Keegan McNamara, Christian Ritzer, Damien C. Weber, Lei Xing, and Carla Winterhalter. Partial-ring PET image correction using implicit neural representation learning. In *XXth International Conference on the use of Computers in Radiation therapy*, Lyon, France, July 2024. 8–11 July 2024.
- [13] Yeqi Fang, Wei Hong, and Jun Tao. Identifying black holes through space telescopes and deep learning. *Phys. Rev. D*, 110:063011, Sep 2024.
- [14] Chang Liu, Yeqi Fang, YuHuan Xie, Hao Zheng, Xin Li, Dongsheng Wu, and Tao Zhang. Deep learning pneumoconiosis staging and diagnosis system based on multi-stage joint approach. *BMC Medical Imaging*, 24(165), jul 2024.
- [15] Andrew J Reader, Guillaume Corda, Abolfazl Mehranian, Casper da Costa-Luis, Sam Ellis, and Julia A Schnabel. Deep learning for pet image reconstruction. *IEEE Transactions on Radiation and Plasma Medical Sciences*, 5(1):1–25, 2020.
- [16] V. S. S. Kandarpa, Alexandre Bousse, Didier Benoit, and Dimitris Visvikis. Dug-recon: A framework for direct image reconstruction using convolutional generative networks. *IEEE Transactions on Radiation and Plasma Medical Sciences*, 5(1):44–53, January 2021.
- [17] Cheng-Cheng Liu and Hsiu-Maan Huang. Partial-ring PET image restoration using a deep learning based method. *Physics in Medicine and Biology*, 64(22):225014, 2019.
- [18] Yuxin Xue, Yige Peng, Lei Bi, Dagan Feng, and Jinman Kim. Cg-3dsrgan: A classification guided 3d generative adversarial network for image quality recovery from low-dose pet images, 2023.
- [19] Andrew J. Reader and Bo Pan. Artificial intelligence for PET image reconstruction. *British Journal of Radiology*, 96(1150):20230292, 2023.
- [20] Rajat Vashistha, Viktor Vegh, Hamed Moradi, Amanda Hammond, Kevin O’Brien, and David Reutens. Modular GAN: PET image reconstruction using two generative adversarial networks. *Frontiers in Radiology*, 4:1466498, 2024.
- [21] Robert Harrison, Steven Gillispie, and Thomas Lewellen. Simulation system for emission tomography (simset): Using simulation to research ideas in emission tomography (pet and spect). *Journal of Nuclear Medicine*, 49(supplement 1):157P–157P, 2008.
- [22] Zeyu Han, Yuhan Wang, Peng Wang, Binyu Yan, Yan Wang, Luping Zhou, Jiliu Zhou, and Ding-gang Shen. Contrastive diffusion model with auxiliary guidance for coarse-to-fine pet reconstruction. In *Medical Image Computing and Computer-Assisted Intervention – MICCAI 2023, LNCS*, volume 14229, pages 239–249. Springer, Cham, 2023.
- [23] Olaf Ronneberger, Philipp Fischer, and Thomas Brox. U-net: Convolutional networks for biomedical image segmentation, 2015.
- [24] Ozan Oktay, Jo Schlemper, Loic Le Folgoc, Matthew Lee, Mattias Heinrich, Kazunari Misawa, Kensaku Mori, Steven McDonagh, Nils Y Hammerla, Bernhard Kainz, Ben Glocker, and Daniel Rueckert. Attention u-net: Learning where to look for the pancreas, 2018.

- [25] Ali Hatamizadeh, Yucheng Tang, Vishwesh Nath, Dong Yang, Andriy Myronenko, Bennett Landman, Holger Roth, and Daguang Xu. Unetr: Transformers for 3d medical image segmentation, 2021.
- [26] Jieneng Chen, Yongyi Lu, Qihang Yu, Xiangde Luo, Ehsan Adeli, Yan Wang, Le Lu, Alan L. Yuille, and Yuyin Zhou. Transunet: Transformers make strong encoders for medical image segmentation, 2021.
- [27] Zeyu Han, Yuhan Wang, Luping Zhou, Peng Wang, Binyu Yan, Jiliu Zhou, Yan Wang, and Ding-gang Shen. Contrastive diffusion model with auxiliary guidance for coarse-to-fine PET reconstruction. In *Medical Image Computing and Computer Assisted Intervention – MICCAI 2023, LNCS*, pages 239–249. Springer, 2023.
- [28] Guido Van Rossum and Fred L. Drake. *Python 3 Reference Manual*. CreateSpace, Scotts Valley, CA, 2009.
- [29] Itseez. Open source computer vision library. <https://github.com/itseez/opencv>, 2015.
- [30] Pauli Virtanen, Ralf Gommers, Travis E. Oliphant, Matt Haberland, Tyler Reddy, David Cournapeau, Evgeni Burovski, Pearu Peterson, Warren Weckesser, Jonathan Bright, Stéfan J. van der Walt, Matthew Brett, Joshua Wilson, K. Jarrod Millman, Nikolay Mayorov, Andrew R. J. Nelson, Eric Jones, Robert Kern, Eric Larson, C J Carey, İlhan Polat, Yu Feng, Eric W. Moore, Jake VanderPlas, Denis Laxalde, Josef Perktold, Robert Cimrman, Ian Henriksen, E. A. Quintero, Charles R. Harris, Anne M. Archibald, Antônio H. Ribeiro, Fabian Pedregosa, Paul van Mulbregt, and SciPy 1.0 Contributors. SciPy 1.0: Fundamental Algorithms for Scientific Computing in Python. *Nature Methods*, 17:261–272, 2020.
- [31] Adam Paszke, Sam Gross, Francisco Massa, Adam Lerer, James Bradbury, Gregory Chanan, Trevor Killeen, Zeming Lin, Natalia Gimelshein, Luca Antiga, Alban Desmaison, Andreas Kopf, Edward Yang, Zachary DeVito, Martin Raison, Alykhan Tejani, Sasank Chilamkurthy, Benoit Steiner, Lu Fang, Junjie Bai, and Soumith Chintala. Pytorch: An imperative style, high-performance deep learning library. In *Advances in Neural Information Processing Systems 32*, pages 8024–8035. Curran Associates, Inc., 2019.
- [32] J. D. Hunter. Matplotlib: A 2d graphics environment. *Computing in Science & Engineering*, 9(3):90–95, 2007.
- [33] Michael L. Waskom. seaborn: statistical data visualization. *Journal of Open Source Software*, 6(60):3021, 2021.